Nonlinear Magnetics Model for Permanent Magnet Synchronous Machines Capturing Saturation and Temperature Effects

Kishan Srinivasan, *Graduate Student Member, IEEE*, Fanny A. Pinto Delgado, *Member, IEEE*, Heath Hofmann, *Fellow, IEEE*, and Jing Sun, *Fellow, IEEE*

***Abstract*—This paper proposes a nonlinear magnetics model for Permanent Magnet Synchronous Machines that accurately captures the effects of magnetic saturation in the machine iron and variations in rotor temperature on the permanent magnet excitation. The proposed model considers the permanent magnet excitation as a current source rather than the more commonly used flux-linkage source. A comparison of the two modeling approaches is conducted using Finite Element Analysis for different machine designs as well as experimental validation, where it is shown that the proposed model has substantially better accuracy. The proposed model decouples the effects of magnetic saturation and rotor temperature variations on the current/flux-linkage relationship, allowing for adaptive estimation of a single parameter to account for rotor temperature changes.**

***Index Terms*—Electric machine modeling, permanent magnet synchronous machines, saturation effects, non-linear magnetics model.**

NOMENCLATURE

$\mathbf{J}$	90° rotation matrix.
i_d^r	Direct axis current in rotor reference frame.
λ_d^r	Direct axis flux linkage in rotor reference frame.
L_d	Direct axis inductance.
v_d^r	Direct axis stator voltage in rotor reference frame.
θ_{re}	Electrical rotor angle.
τ_{em}	Electromagnetic torque.
Φ_{pm}	Flux due to permanent magnet.
ϕ	Flux.
$\mathbf{L}$	Inductance matrix.
$\mathcal{F}$	Magneto-motive force (MMF)
N_p	Number of poles.
I_{pm}	Permanent magnet current.
Λ_{pm}	Permanent magnet flux linkage.
i_q^r	Quadrature axis current in rotor reference frame.
λ_q^r	Quadrature axis flux linkage in rotor reference frame.
L_q	Quadrature axis inductance.
v_q^r	Quadrature axis stator voltage in rotor reference frame.
$\mathcal{R}$	Reluctance.
T_r	Rotor temperature.
R	Stator winding resistance.

Received 22 October 2024; revised 14 March 2025 and 3 July 2025; accepted 13 August 2025. Date of publication 18 August 2025; date of current version 23 February 2026. This work was supported by the Office of Naval Research under Grant N00014-18-1-2330. Paper no. TEC-01213-2024. *(Corresponding author: Kishan Srinivasan.)*

Kishan Srinivasan and Heath Hofmann are with the Department of Electrical Engineering and Computer Science, University of Michigan, Ann Arbor MI 48109 USA (e-mail: kishans@umich.edu).

Jing Sun is with the Department of Naval Architecture and Marine Engineering, University of Michigan, Ann Arbor MI 48109 USA.

Fanny A. Pinto Delgado is with the Research and Development Mercedes BenZ, Ann Arbor MI 48108 USA.

Color versions of one or more figures in this article are available at https://doi.org/10.1109/TEC.2025.3599748.

Digital Object Identifier 10.1109/TEC.2025.3599748

I. Introduction

PERMANENT Magnet Synchronous Machines (PMSMs) have become the popular choice in applications such as vehicle electrification [1], [2], [3], [4], [5], [6], [7], [8], [9]. With recent advances in cooling techniques, it is now possible to develop PMSM designs with very high operating current density, and hence power density [10], [11], [12]. At these high current excitation levels, PMSMs tend to exhibit significant nonlinear (NL) behavior due to saturation of their soft magnetic material. Furthermore, the remanent flux density of Neodymium-Iron-Boron (NdFeB) permanent magnets (PMs) can decrease significantly with increasing rotor temperature [13]. References [14], [15], [16], [17], [18], [19] demonstrate that both magnetic saturation and rotor temperature variation can significantly affect the magnetic properties of the machine, and hence its torque production capability. Thus, it is crucial to accurately capture these phenomena in machine models used for control purposes. The most common control-oriented model for PMSMs is the linear magnetics model, where the flux-linkage/current relationship ($\vec{\lambda}^r$ - $\vec{i}^r$) in the rotor reference frame is modeled with an inductance matrix ($\mathbf{L}$) and a permanent magnet flux linkage source (Λ_{PM}) [20], [21], [22].

$$\vec{\lambda}^r = \mathbf{L}\vec{i}^r + \vec{\lambda}^r_{pm}; \tag{1}$$

$$\mathbf{L} = \begin{bmatrix} L_d & 0 \\ 0 & L_q \end{bmatrix}, \qquad \vec{\lambda}^r = \begin{bmatrix} \lambda_d^r \\ \lambda_q^r \end{bmatrix}, \qquad \vec{i}^r = \begin{bmatrix} i_d^r \\ i_q^r \end{bmatrix},$$

$$\vec{\lambda}^r_{pm} = \begin{bmatrix} \Lambda_{PM} \\ 0 \end{bmatrix}. \tag{2}$$

Linear models become inaccurate when the machine iron is magnetically saturated [22], [23]. In the literature, many different control-oriented models for PMSMs have been attempted

to capture nonlinear magnetic properties under certain assumptions [23], [24], [25], [26], [27], [28], [29], [30], [31], [32], [33], [34]. However, these approaches do not take into account the effects of rotor temperature.

Typically, the effects of temperature variation are considered solely based on the temperature variation of the permanent magnets while neglecting the effects of temperature on the soft magnetic material properties. This is because of the lower Curie temperature of NdFeB magnets compared to soft magnetic materials, which makes them much more sensitive to changes in temperature. Many approaches that capture rotor temperature effects therefore model inductances [35], [36] as a function of rotor reference frame currents i_d^r and i_q^r to capture the saturation phenomenon, while the permanent magnet excitation is modeled as a flux linkage source $\Lambda_{PM}(T_r)$ whose value varies with rotor temperature. This separation of magnetic saturation and rotor temperature effects in the model is useful as it allows for the PM flux linkage to be treated as a parameter that can be adaptively estimated in real time, thereby tracking changes due to rotor temperature. However, it has been shown that this approach becomes inaccurate in regions of heavy magnetic saturation and significant variation in rotor temperature [27].

In an attempt to improve accuracy, [16], [37] propose forming three-dimensional Look-Up Tables (LUTs) with currents as a function of both flux linkages and rotor temperature; i.e., $\vec{i}^r = f(\vec{\lambda}^r, T_r)$. Another approach is to calculate the inductance matrix as a function of rotor temperature and currents from a three-dimensional LUT. Authors in [15] have also suggested to include compensation terms to take into account rotor temperature variation in the LUT, which primarily captures saturation. All of these approaches suffer from the need for additional model parameters that depend upon rotor temperature. This requires either the knowledge of the rotor temperature, through measurement or estimation, or the application of adaptive techniques that estimate multiple parameters simultaneously, which relies on a persistent excitation condition to ensure parameter convergence [38].

Another approach to improving accuracy involves using Finite Element Analysis (FEA) models, or reduced-order models formed from FEA models [39], [40], [41]. This approach also require knowledge of rotor temperature. Moreover, obtaining accurate FEA models of actual PMSMs requires knowledge of the dimensional parameters and material properties of the machine, information which is not often available to the controls engineer.

An alternate approach to modeling permanent magnet excitation is through the use of a current source rather than a flux-linkage source, as discussed in [8], [42], [43]. However, the models in these papers all assume linear magnetics, hence they do not address the issue of accurate modeling of the effects of magnetic saturation and rotor temperature variations. In this paper, we present a magnetics model for PMSMs that accurately captures both the nonlinear and rotor-temperature-dependent behavior of PMSMs by modeling the PM as a current source as opposed to the typical flux linkage source. A key contribution of this model is the decoupling of the nonlinear effects of magnetic saturation and the rotor temperature effect on permanent magnet excitation.

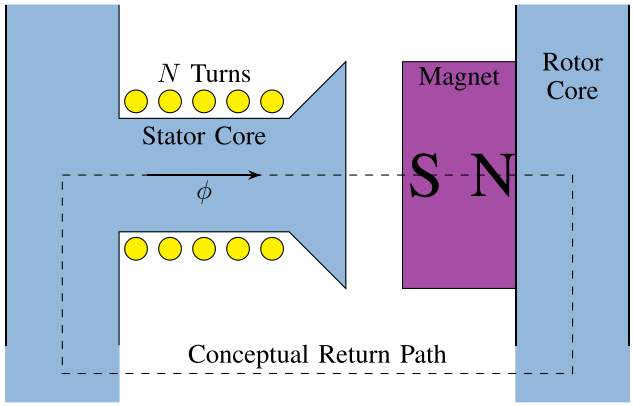

Fig. 1. Simplified, single-coil magnetics model of PMSM machine.

In this model magnetic saturation can be captured through the use of two two-dimensional LUTs and the permanent magnet excitation can be captured in a single parameter, the permanent magnet current. This parameter can then be adaptively estimated in real time, removing the need for measurement or estimation of the rotor temperature. The result is an accurate model suitable for use in real-time control that works over a broad operating range, and is computationally efficient and relatively simple to implement. Table I compares the structure of the proposed model with models from literature.The proposed PMSM model is introduced and justified in Section II. A comparison of the proposed model with a representative nonlinear model that uses a PM flux linkage parameter is conducted in III-B using FEA simulation results for different machine designs. A similar comparison is conducted using experimental data in IV, followed by concluding remarks in V.

II. Proposed Model

A. Model Development

The motivation for the proposed model is illustrated by considering the single-coil magnetic model shown in Fig. 1.

We begin by creating a magnetic circuit model. The N-turn coil is represented by an magnetomotive force (MMF) source Ni, where i is the current flowing in the coil. The stator and rotor cores consist of a soft magnetic material exhibiting magnetic saturation, and so are represented by a nonlinear reluctance $\mathcal{R}_c(\phi)$ whose value varies with flux level ϕ. The PM is assumed to possess linear magnetic properties with an incremental permeability μ_m and a remanent flux density B_r that varies with rotor temperature T_r, and so is modeled as a constant reluctance $\mathcal{R}_{pm}$ and flux source $\Phi_{pm}(T_r)$, as shown in Fig. 2.

An equivalent magnetic circuit can be created using the Thevenin equivalent of the PM, where the PM excitation is modelled as an MMF source $\mathcal{F}_{pm}(T_r) = \mathcal{R}_{pm}\Phi_{pm}(T_r)$ rather than a flux source. Simplifying the magnetic circuit further, the two reluctances are now in series and can be combined into a single nonlinear reluctance, $\mathcal{R}_{tot}(\phi)$. Analysis of the resulting magnetic circuit yields:

$$Ni + \mathcal{F}_{pm}(T_r) = \mathcal{R}_{tot}(\phi)\phi. \tag{3}$$

TABLE I
COMPARISON OF STRUCTURE OF THE PROPOSED MODEL WITH MODELS IN LITERATURE

Reference	Model	Effects of Rotor Temperature	Parameter Count	Look-Up Tables	Comments
[20], [21], [22]	Linear	Yes	3 (L_d, L_q and Λ_{pm})	none	Does not capture magnetic saturation
[42], [43], [8]	Linear	No	3 (L_d, L_q and I_{pm})	none	Does not capture magnetic saturation
[24], [23], [25], [26] [27], [28], [29], [30] [31], [32], [33], [34]	NL	No	1 (Λ_{pm})	Two 2D	Does not capture rotor temperature effects
[35], [36]	NL	Yes	1 (Λ_{pm})	Two 2D	Inaccurate in the region of deep magnetic saturation and significant rotor temperature variation [27]
[16], [37]	NL	Yes	-	Minimum of two 3D	Requires higher dimensional LUT; Rotor temperature needs to be measured or estimated
Proposed model	NL	Yes	1 (I_{pm})	Two 2D	Decouples magnetic saturation and effects of rotor temperature variation; Knowledge of rotor temperature unnecessary through online I_{pm} estimation

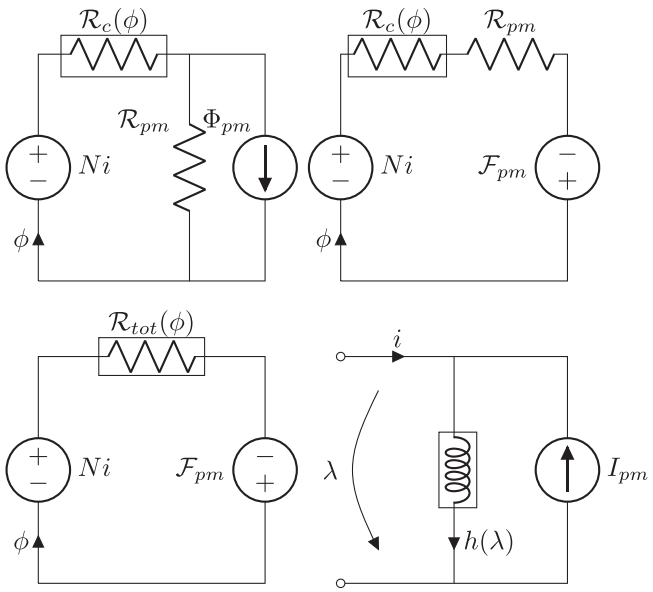

Fig. 2. Derivation of proposed magnetics model for single-coil. Top left: magnetic circuit model. Top right: Thevenin equivalent of permanent magnet. Bottom left: Combination of magnet and core reluctances. Bottom right: Resulting electric circuit model.

If we denote $f(\phi) = \mathcal{R}_{tot}(\phi)\phi$, and note that $\phi = \frac{\lambda}{N}$, we can represent the current as follows:

$$i = \frac{1}{N}\left(f\left(\frac{\lambda}{N}\right) - \mathcal{F}_{pm}(T_r)\right) \tag{4}$$

$$= h(\lambda) - I_{pm}(T_r). \tag{5}$$

This expression can be represented in an electrical circuit model as a nonlinear inductance, with current/flux-linkage relationship $i = h(\lambda)$, in parallel with a current source $I_{pm}(T_r)$ representing the PM excitation, as shown in Fig. 2. As the value of I_{pm} is directly proportional to the remanent flux density B_r of the magnet, it will share the same dependence upon the rotor temperature.

In order to illustrate the advantages of the proposed model, we consider a model consisting of a nonlinear inductance and the more commonly used flux-linkage source representing permanent magnet excitation.

$$\lambda = \mathbf{L}(i)i + \Lambda_{pm}(T_r). \tag{6}$$

The key distinction between the two models is how the current/flux-linkage relationships react to changes in rotor temperature. In the case of the model (6) with a PM flux linkage source, the result of a rotor temperature change would be a constant offset $\Delta\Lambda$ in the $\lambda - i$ curve. In the case of the proposed model a change in rotor temperature would result in a constant offset ΔI.

Fig. 3 shows a representative flux linkage/current relationship at two different rotor temperatures. One figure plots flux linkage versus current, the other current versus flux linkage, both represent the same data.

As can be seen, the variation of the $\lambda - i$ curve with temperature is not captured well by a constant offset in the flux linkage as modeled in (6). This is because the saturation effect results in a convergence of the flux-linkage values at high current excitation. However, the variation of the $i - \lambda$ curve is well captured by a constant offset in current as seen in Fig. 3(b) and hence is captured well by the model presented in (5).

B. Proposed Permanent Magnet Synchronous Machine Model

The proposed equivalent two-phase model for a Permanent Magnet Synchronous Machine (PMSM) is developed considering the standard smooth-airgap model (i.e., effects due to the slots in the stator core are neglected).

1) Current/flux-Linkage Relationship: The current/flux-linkage relationships of the proposed machine model are presented in the rotor reference frame (designated by a superscript 'r'), which is related to the variables in the stationary reference frame as follows:

$$\vec{x}^r = e^{-\mathbf{J}\theta_{re}}\vec{x}, \quad \vec{x} = e^{\mathbf{J}\theta_{re}}\vec{x}^r. \tag{7}$$

where $\theta_{re} = \frac{N_p}{2}\theta_r$ is the electrical rotor angle,

$$\mathbf{J} = \begin{bmatrix} 0 & -1 \\ 1 & 0 \end{bmatrix}$$

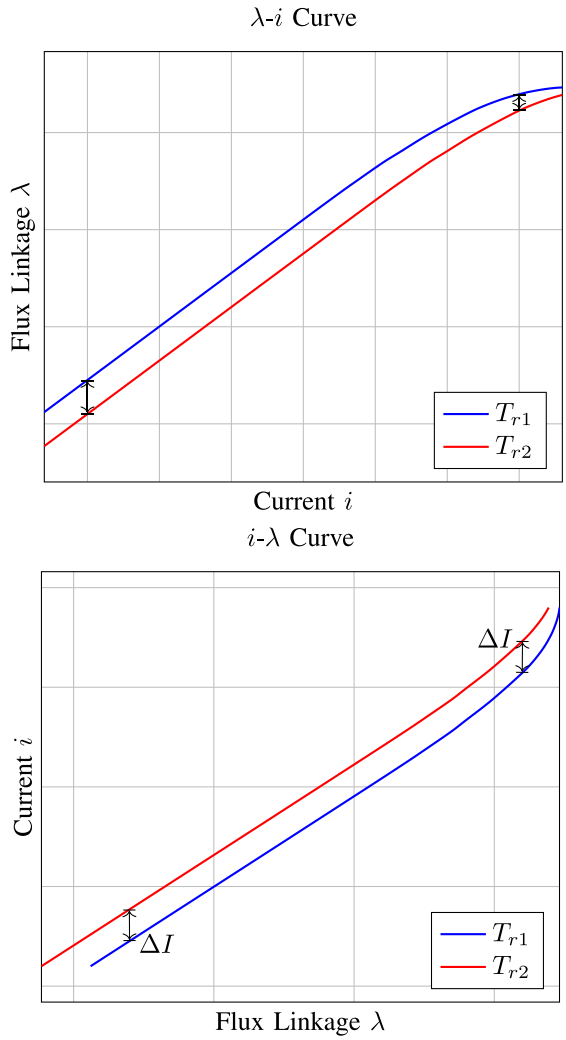

Fig. 3. Representative flux-linkage/current relationship capturing magnetic saturation at two different rotor temperatures. Top: $\lambda - i$ curve. Bottom: $i - \lambda$ curve.

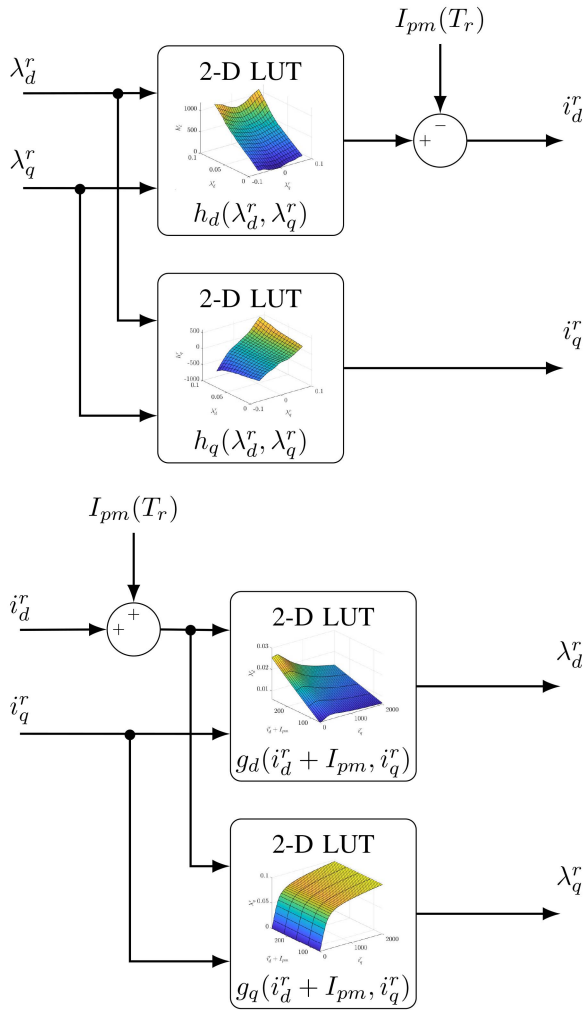

Fig. 4. Example implementations of the proposed magnetics model using two-dimensional lookup tables. Top: flux linkage to current mapping. Bottom: current to flux linkage mapping.

is the 90° rotation matrix, N_p is the number of poles of the machine, and θ_r is the mechanical angle of the rotor. The matrix exponentials $e^{-\mathbf{J}\theta_{re}}$ and $e^{\mathbf{J}\theta_{re}}$ represent the Park and Inverse Park Transforms, respectively.

The current/flux-linkage relationships are an extension of the single-coil model discussed in the prequel to a vector representation:

$$\vec{i}^r = \vec{h}\left(\vec{\lambda}^r\right) - \vec{i}^r_{pm}(T_r) \tag{8}$$

or

$$\begin{bmatrix} i_d^r \\ i_q^r \end{bmatrix} = \begin{bmatrix} h_d(\lambda_d^r, \lambda_q^r) \\ h_q(\lambda_d^r, \lambda_q^r) \end{bmatrix} - \begin{bmatrix} I_{pm}(T_r) \\ 0 \end{bmatrix} \tag{9}$$

where I_{pm} represents the permanent magnet excitation.

The mapping $\vec{h}(\vec{\lambda}^r)$ captures the nonlinear effects of saturation of soft magnetic materials of the machine. and has the following property

$$\vec{h}(\vec{0}) = \vec{0}. \tag{10}$$

If the electric machine design has the standard symmetries, $\vec{h}(\vec{\lambda}^r)$ also has the following properties:

$$h_d(\lambda_d^r, -\lambda_q^r) = h_d(\lambda_d^r, \lambda_q^r), \tag{11}$$

$$h_q(\lambda_d^r, -\lambda_q^r) = -h_q(\lambda_d^r, \lambda_q^r). \tag{12}$$

Assuming standard magnetic material properties (e.g., incremental permeabilities are always positive), it can be shown that $\vec{h}(\vec{\lambda}^r)$ is injective and surjective, and so an inverse flux-linkage/current relationship exists:

$$\vec{\lambda}^r = \vec{h}^{-1}\left(\vec{i}^r + \vec{i}^r_{pm}\right) = \vec{g}\left(\vec{i}^r + \vec{i}^r_{pm}\right). \tag{13}$$

Example implementations of the proposed magnetics model and its inverse relationship using two-dimensional lookup tables are shown in Fig. 4. Techniques for determining the datapoints in the lookup tables and the PM current as a function of rotor temperature will be discussed in detail in the sequel.

A test was conducted to compare the computational efficiency of two-dimensional versus three-dimensional lookup tables,

such as those used in the models presented in [16] and [37]. The computation times of two 2D (36x41) lookup tables and two 3D lookup tables (36x41x5) were calculated by performing random lookups throughout the range of the tables. These calculations were performed in MATLAB using the 'interp2' and 'interpn' functions and linear interpolation on a computer with an Intel Xeon 3.2 GHz processor and 12 GB RAM. Ten million lookups were performed to obtain an average computation time. The 2D lookup tables averaged 32 ns per lookup, whereas the 3D lookup tables averaged 65 ns per lookup.

2) Stator Voltage Dynamic Equations in Rotor Reference Frame: It can be shown that the dynamic stator voltages can be presented in vector and scalar form as follows:

$$\vec{v}^r = R\vec{i}^r + \frac{N_p}{2}\omega_r \mathbf{J}\vec{\lambda}^r + \frac{d\vec{\lambda}^r}{dt} \tag{14}$$

$$= R\left[\vec{h}\left(\vec{\lambda}^r\right) - \vec{i}^r_{pm}\right] + \frac{N_p}{2}\omega_r \mathbf{J}\vec{\lambda}^r + \frac{d\vec{\lambda}^r}{dt}, \tag{15}$$

$$v^r_d = R\left[h_d\left(\vec{\lambda}^r\right) - I_{pm}\right] - \frac{N_p}{2}\omega_r \lambda^r_q + \frac{d\lambda^r_d}{dt},$$

$$v^r_q = Rh_q\left(\vec{\lambda}^r\right) + \frac{N_p}{2}\omega_r \lambda^r_d + \frac{d\lambda^r_q}{dt} \tag{16}$$

where ω_r is the angular velocity of the rotor and R is the winding resistance.

3) Electromagnetic Torque: As stated in [29], the electromagnetic torque is the cross product of the flux linkage and the current. Thus, the torque expression for the proposed model can be shown as:

$$\tau_{em} = \frac{3N_p}{4}\left[\lambda^r_d i^r_q - \lambda^r_q i^r_d\right],$$

$$\tau_{em} = \frac{3N_p}{4}\left[h_q\left(\vec{\lambda}^r\right)\lambda^r_d - h_d\left(\vec{\lambda}^r\right)\lambda^r_q + I_{pm}\left(T_r\right)\lambda^r_q\right], \tag{17}$$

where the first two terms in (17) correspond to a (nonlinear) reluctance torque and the final term is the PM torque.

III. Validation and Comparison Results

In this section we will illustrate the accuracy of the proposed model through comparison with a "baseline" PM flux-linkage model. We will first introduce the baseline model. We will then compare how changes in the rotor temperature affect the accuracy of the proposed and baseline models. The first comparisons will be conducted using FEA results for three different machine designs: an interior permanent machine, a distributed-winding surface mount permanent magnet (SMPM) machine, and a concentrated-winding SMPM machine. Finally, a comparison will be conducted using experimental results.

A. Baseline Model

We will use the following nonlinear PM flux linkage model as a baseline for comparison with the proposed model:

$$\vec{\lambda}^r = \vec{f}(\vec{i}^r) + \vec{\lambda}^r_{pm}(T_r), \tag{18}$$

where,

$$\vec{f}(\vec{i}^r) = \begin{bmatrix} f_d(i^r_d, i^r_q) \\ f_q(i^r_q, i^r_q) \end{bmatrix}, \qquad \vec{\lambda}^r_{pm}(T_r) = \begin{bmatrix} \Lambda_{PM}(T_r) \\ 0 \end{bmatrix}$$

and the torque is given by

$$\tau_{em} = \frac{3N_p}{4}\left[\lambda^r_d i^r_q - \lambda^r_q i^r_d\right],$$

$$= \frac{3N_p}{4}\left[f_d(i^r_d, i^r_q) i^r_q + \Lambda_{pm}(T_r) i^r_q - f_q(i^r_d, i^r_q) i^r_d\right]. \tag{19}$$

This particular model was chosen for comparison as it uses the conventional permanent magnet flux linkage source to capture the permanent magnet excitation, yet separates the effects of non-linear saturation behavior and rotor temperature variation in a similar way as the proposed nonlinear PM current model.

B. Model Comparison Using FEA-Based Data

We first use two-dimensional finite element analysis (FEA) results from ANSYS as the basis for comparison. The process used to compare the two models is as follows:

1) Using FEA, calculate the flux linkages λ^r_d and λ^r_q and the electromagnetic torque τ_{em} over a range of currents i^r_d and i^r_q with the rotor temperature set at $T_1 = 20°C$.
2) Use the flux-linkage/current data to determine the values of $I_{pm}(T_1)$ (used in the proposed model) and $\Lambda_{pm}(T_1)$ (used in the baseline model). The value of Λ_{pm} is determined from λ^r_d by setting the currents to zero, and the value of I_{pm} is determined by finding the value of i^r_d that sets $\lambda^r_d = 0$ ($I_{pm} = \| - i^r_d \|$).
3) Generate a look-up table for the $\vec{\lambda}^r = \vec{g}(\vec{i}^r + \vec{i}^r_{pm})$ mapping of the proposed model using $20°C$ FEA data. Note that we determine the $\vec{g}(\cdot)$ mapping rather than the $\vec{h}(\cdot)$ mapping in order to more easily enable the comparison.
4) Generate a look-up table for $\vec{f}(\vec{i}^r)$ in the baseline model using the $20°C$ FEA data.
5) Repeat steps 1) and 2) for a different rotor temperature (T_2).
6) Compute the flux linkages and torques with the proposed model using the nonlinear look-up table for $\vec{g}(\cdot)$ determined from the T_1 data and $I_{pm}(T_2)$.
7) Compute the flux linkages and torques with the comparison model using the nonlinear look-up table $\vec{f}(\vec{i}^r)$ from the T_1 data and $\Lambda_{pm}(T_2)$ for the baseline model.
8) Compare the results from the previous steps 6) and 7) with the FEA results at the new rotor temperature (T_2).

1) Interior Permanent Magnet Machine: We first consider the interior permanent magnet machine design presented in [44] and shown in Fig. 5(a).

The permanent magnet material parameters used are for NdFeB N35UH from Arnold Magnetics [13]. The mechanical dimensions and winding parameters are kept the same as in [44]. With recent advancements in cooling as shared in [45], peak current densities of 48 A_{rms}/mm^2 can be achieved in electric machines. We use this value to determine the maximum current of the mapping, though we note that this machine was not specifically designed for these current densities. An example

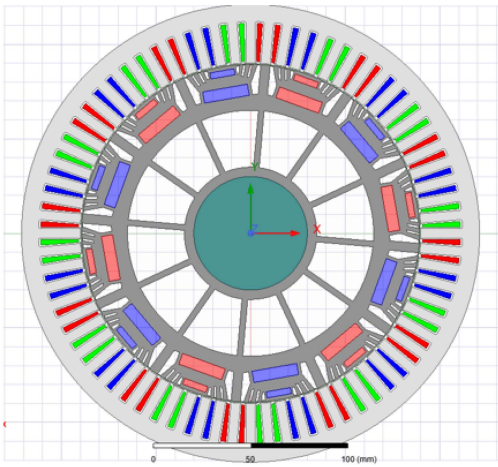

Fig. 5. (a) Cross-section of Interior Permanent Magnet machine [44]. (b) Flux density plot calculated using FEA.

TABLE II
I_{pm} AND Λ_{pm} VALUES FOR INTERIOR PERMANENT MAGNET MACHINE

Rotor Temperature ($^\circ C$)	I_{pm} (A)	$\Lambda_{pm}(V-s)$
20	264.8	0.0256
60	245.6	0.0238
80	235.1	0.0227
100	225.4	0.0219

magnetic flux density distribution for this machine design is shown in Fig. 5(b).

The nonlinear $\vec{\lambda}^r$ - $\vec{i}^r$ mapping, determined using FEA at temperatures T_1=20$^\circ C$ and T_2=100$^\circ C$, is shown in Fig. 6.

As is to be expected, we see a significant change in λ_d^r whereas λ_q^r is not substantially different. The value of I_{pm} and Λ_{pm} was determined for multiple temperatures and is shown in Table II.The absolute errors in λ_d^r and λ_q^r at $T_2 = 100^\circ C$ for both the proposed PM current model and the baseline PM flux linkage model are shown in Figs. 7 and 8.

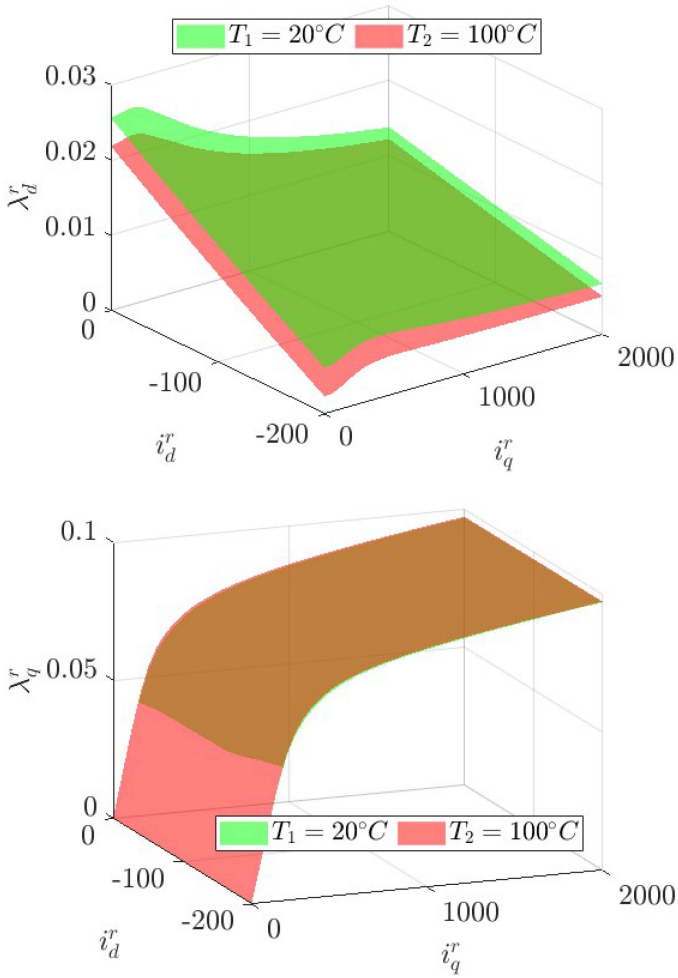

Fig. 6. $\vec{\lambda}^r$ - $\vec{i}^r$ mapping of interior permanent magnet machine at different rotor temperatures (FEA results). Top: λ_d^r mapping. Bottom: λ_q^r mapping.

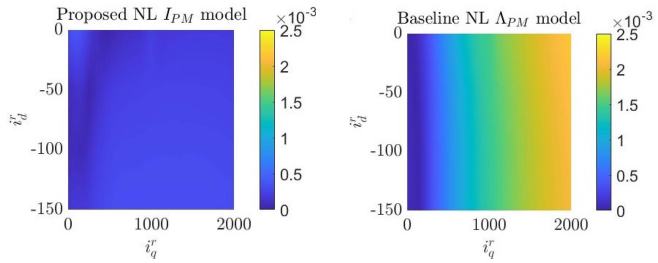

Fig. 7. Absolute errors in λ_d^r for Interior Permanent Magnet machine at $T = 100^\circ C$ for the proposed (left) and baseline (right) models, FEA results.

It can be seen that the baseline PM flux linkage model experiences significantly larger error in λ_d^r at high values of i_q^r when compared to the proposed PM current model. In the case of λ_q^r, the model errors are similar, and occur at the onset of magnetic saturation on the quadrature axis.

The relative error in torque for the two models is highlighted in Fig. 9.

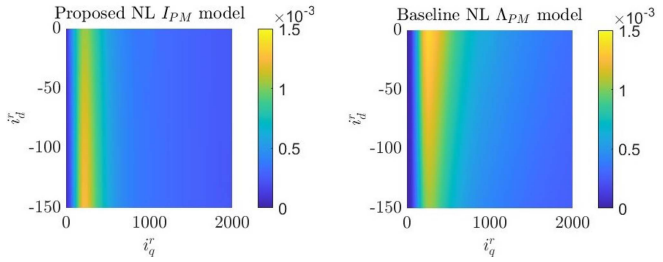

Fig. 8. Absolute errors in λ_q^r for Interior Permanent Magnet machine at $T = 100°C$ for the proposed (left) and baseline (right) models, FEA results.

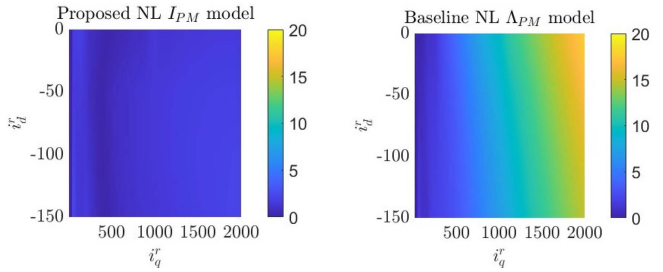

Fig. 9. Relative torque errors (in %) for Interior Permanent Magnet machine at $T = 100°C$ for proposed (left) and baseline (right) models, FEA results.

TABLE III
DISTRIBUTED WINDING SMPM PARAMETERS

Parameter	Value
Number of poles	4
Number of slots	24
Conductors per slot	100
Parallel branches	1
Magnet material	NdFe35 (N35UH)
Steel type	M19 24G
Stator outer diameter (mm)	160
Stator inner diameter (mm)	80
Rotor outer diameter (mm)	78
Magnet thickness (mm)	5
Machine length (mm)	80

It can be clearly seen that the proposed PM current model shows a significant improvement in torque accuracy when compared to the PM flux linkage model, especially at high values of i_q^r when the machine iron is heavily saturated.

2) Distributed-Winding SMPM Machine: A 4 pole, distributed winding SMPM (Fig. 10(a)) with machine parameters as shown in Table III is simulated in ANSYS FEA for rotor temperatures $T_1 = 20°C$ and $T_2 = 120°C$. The magnetic flux density plot is shown in Fig. 10(a). The machine is simulated with current density of $13\text{A}_{rms}/\text{mm}^2$, which corresponds to forced-air cooling conditions. It can be seen that the proposed PM current model again outperforms the PM flux linkage model.

The values of I_{pm} and Λ_{pm} for different rotor temperatures are provided in Table IV for this machine design.

Fig. 11 through 13 show absolute errors in λ_d^r and λ_q^r and the relative torque error for the two models at temperature T_2. It can be seen that, for λ_d^r and hence torque, significant errors occur for negative values of i_d^r. This is due to the fact that the machine iron is saturated by the permanent magnets at zero current excitation.

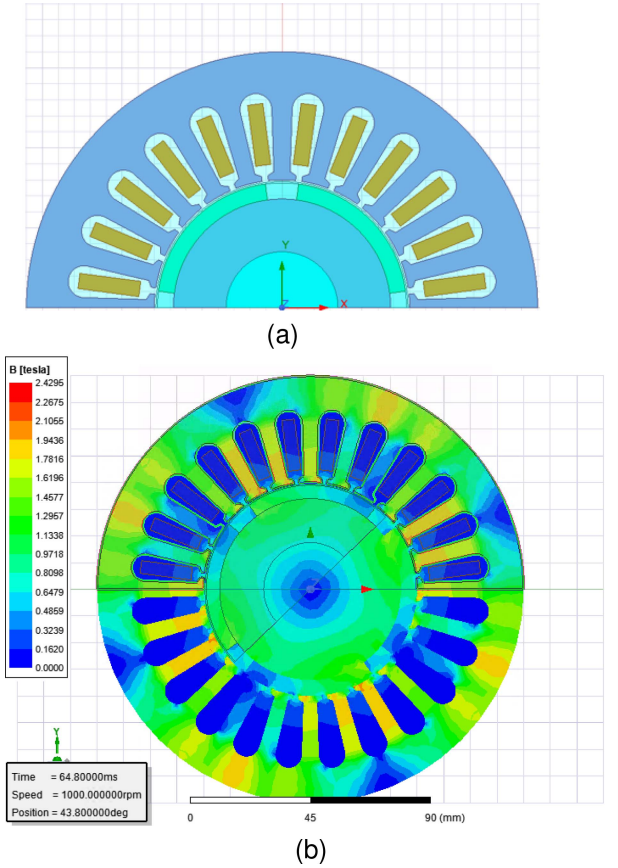

Fig. 10. (a) Cross-section of Distributed winding SMPM machine in ANSYS Maxwell. (b) Flux density plot calculated using FEA.

TABLE IV
I_{pm} AND Λ_{pm} VALUES FOR DISTRIBUTED WINDING SMPM MACHINE

Rotor Temperature ($°C$)	I_{pm} (A)	$\Lambda_{pm}(V-s)$
20	40.38	1.2643
60	38.4	1.2281
80	37.3	1.2048
100	36.3	1.1842
120	35.1	1.156

The field-weakening effect of negative i_d^r drives the iron out of saturation and so causes the effective PM flux linkage to increase, resulting in the error.

3) Concentrated-Winding SMPM Machine: A 4-pole concentrated winding SMPM machine with parameters shown in Table V is simulated in ANSYS FEA for rotor temperatures $T_1 = 20°C$ and $T_2 = 100°C$. The machine is simulated with a peak current density of $35.5\text{A}_{rms}/\text{mm}^2$, corresponding to liquid cooling conditions. The machine cross section is shown in Fig. 14(a), and the flux density plot for this design is shown in Fig. 14(b).

The I_{pm} and Λ_{pm} values for this machine as a function of rotor temperature are provided in Table VI.

The absolute error in λ_d^r and λ_q^r for both models is compared as shown in Figs. 15 and 16. The relative error in torque by both models is compared in Fig. 17. We can clearly observe the improvement in accuracy in the proposed model from Figs. 15

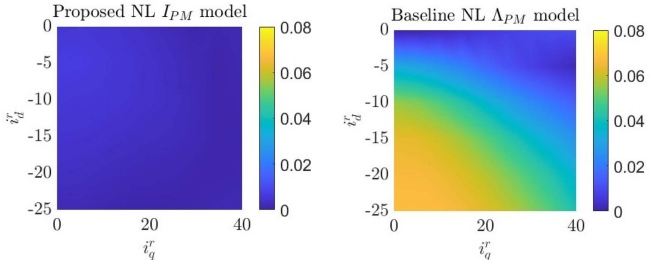

Fig. 11. Absolute errors in λ_d^r for distributed winding SMPM at $T = 120°C$ for proposed (left) and baseline (right) models, FEA results.

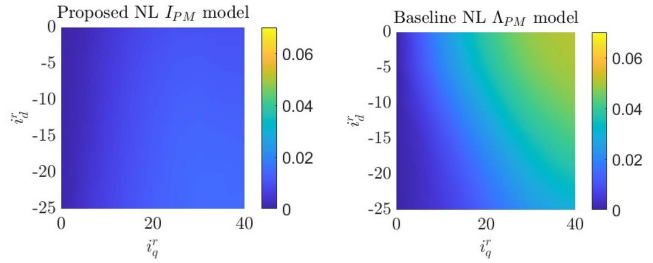

Fig. 12. Absolute errors in λ_q^r for distributed winding SMPM at $T = 120°C$ for proposed (left) and baseline (right) models, FEA results.

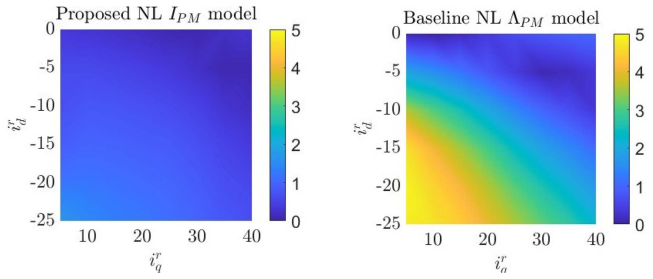

Fig. 13. Relative torque errors (in %) for distributed winding SMPM at $T = 120°C$ for proposed (left) and baseline (right) models, FEA results.

TABLE V
CONCENTRATED WINDING SMPM PARAMETERS

Parameter	Value
Number of poles	4
Number of slots	6
Conductors per slot	220
Parallel branches	1
Magnet material	NdFe35 (N35UH)
Steel type	M19 24G
Stator outer diameter (mm)	175
Stator inner diameter (mm)	80
Rotor outer diameter (mm)	74
Magnet thickness (mm)	3
Machine length (mm)	80

TABLE VI
I_{pm} AND Λ_{pm} VALUES FOR CONCENTRATED WINDING SMPM MACHINE

Rotor Temperature ($°C$)	I_{pm} (A)	$\Lambda_{pm}(V-s)$
20	26.6167	0.399
60	25.3747	0.3809
80	24.6345	0.3698
100	24.0188	0.3605

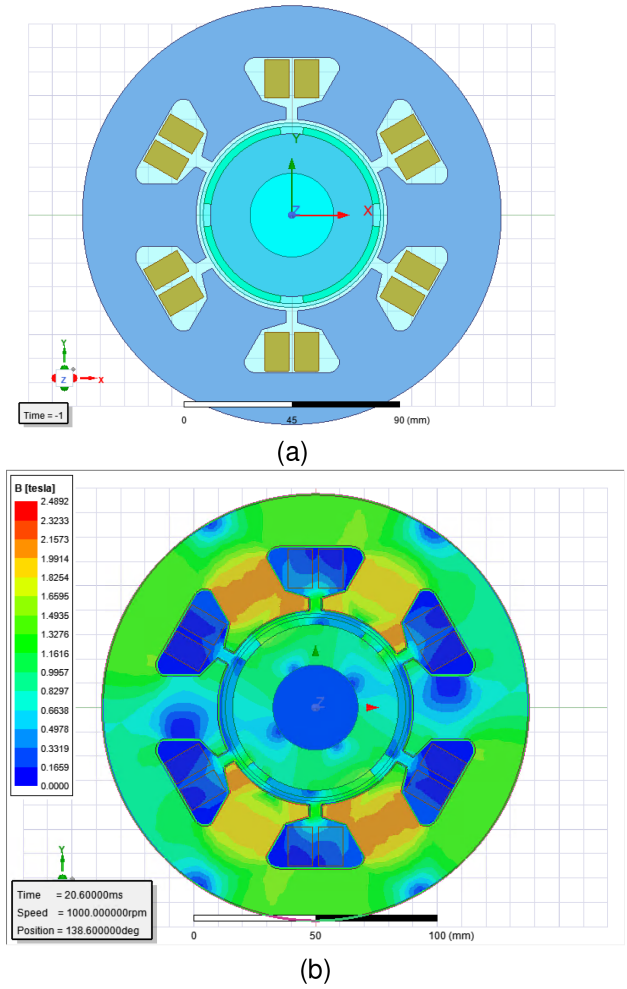

Fig. 14. (a) Cross-section of concentrated winding SMPM machine in ANSYS Maxwell. (b) Flux density plot calculated using FEA.

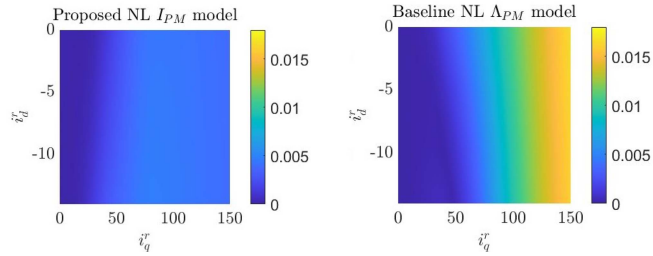

Fig. 15. Absolute errors in λ_d^r for concentrated winding SMPM at $T = 100°C$ for proposed (left) and baseline (right) models, FEA results.

and 17, especially in the region of high torque where magnetic saturation is most prominent.

IV. EXPERIMENTAL VALIDATION

A. Setup

A three-phase, eighteen-pole, 145 kW SMPM from Unique Mobility (UQM) with specifications as shown in Table VII was characterized using a dSpace Scalexio real-time target controller

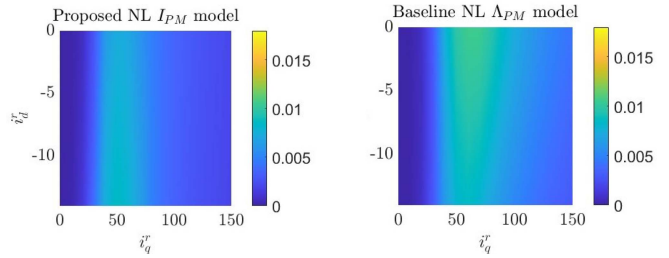

Fig. 16. Absolute errors in λ_q^r for concentrated winding SMPM at $T = 100°C$ for proposed (left) and baseline (right) models, FEA results.

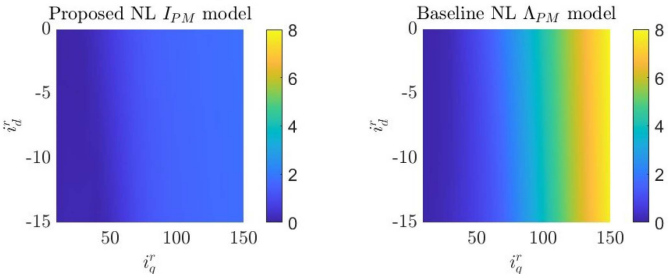

Fig. 17. Relative torque errors (in %) for concentrated winding SMPM at $T = 100°C$ for proposed (left) and baseline (right) models, FEA results.

TABLE VII
TEST MACHINE RATING

Description	Value
Number of poles	18
Manufacturer	UQM Technologies
Type	PM Brushless
Maximum speed	8000rpm
Maximum Current	500A
Maximum Voltage	450V
Rated Power	145KW peak/ 85 KW continuous

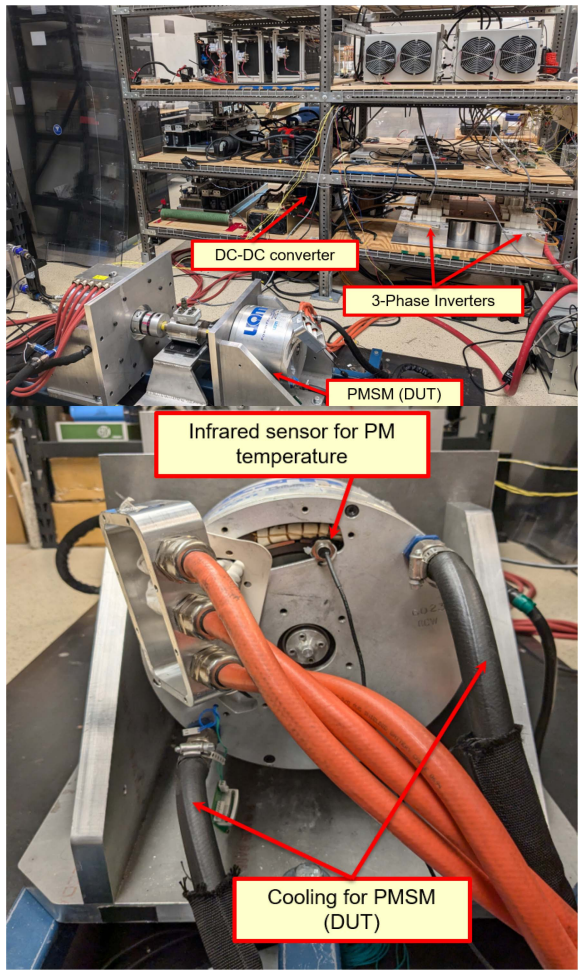

Fig. 18. Top: Hardware setup for experiment, Bottom: Infrared sensor for rotor temperature measurement on the SMPM test machine.

and a three-phase voltage source inverter consisting of SKiiP 1814 GB17E4-3DUW V2 IGBTs, made by Semikron, is used with a switching frequency of 10 kHz, bus voltage of 175 V, and dead time of 2 μs. Space-Vector Modulation (SVM) is used as the modulation scheme to calculate the desired duty cycles. The rotor speed is kept constant at 500 rpm by an electric-machine-based dynamometer. This speed was chosen as the voltage/current relationships of the machine are relatively insensitive to both winding and core losses at the corresponding electrical frequency (75 Hz). An infrared temperature sensor from Texense (IRN2) is used to measure the temperature of the magnets on the rotor. This sensor is pointed at the permanent magnets on the rotor of the machine, which effectively form a solid ring in this machine design. While this approach captures a surface temperature of the magnet rather than an internal or average temperature, the purpose of the IR temperature measurement is to establish different rotor temperature conditions in our experiments for the purposes of comparison of the magnetic models, not necessarily to determine an accurate temperature. The measurement, modeling, and estimation of rotor temperature is outside the scope of this manuscript.

Since it is difficult to keep the rotor temperature constant, efforts were made to collect data quickly to keep the temperature variation within 5 °C of the stated value. The experimental setup of the hardware is shown in Fig. 18.

B. Characterization Procedure

The goal of the proposed procedure is to characterize the steady-state flux linkages in the rotor reference frame as a function of direct and quadrature currents and rotor temperature.

A characterization process similar to that provided in [46], [47] is used where the flux linkage can be estimated by integrating the electromotive force (EMF) of the windings, which can be estimated as follows:

$$\vec{\lambda} = \int (\tilde{\vec{v}} - \vec{v}_{RDT}) dt, \tag{20}$$

where $\tilde{\vec{v}}$ is the command voltage from the controller and

$$\vec{v}_{RDT} = R\vec{i} + \vec{v}_t + \vec{v}_{dead}, \tag{21}$$

where $\vec{v}_t(t)$ is the transistor voltage drop and $\vec{v}_{dead}(t)$ is the effective voltage drop due to the dead-time effect in the inverter.

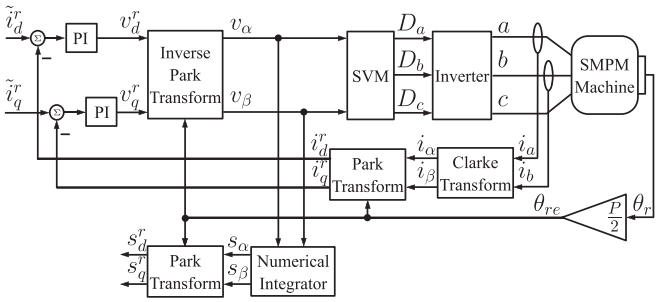

Fig. 19. Data acquisition and controller block diagram for recording the integrated voltages at different current operating conditions.

In the following we will approximate the RDT voltage with its fundamental component $\vec{v}_{1RDT}$, which can be represented as a nonlinear function of the current vector $\vec{i}$ as follows:

$$\vec{v}_{RDT} \approx \vec{v}_{1RDT} = V_{1RDT}\left(\|\vec{i}\|\right)\frac{\vec{i}}{\|\vec{i}\|}, \tag{22}$$

i.e., the magnitude of $\vec{v}_{RDT}$ is a nonlinear function of the current magnitude, and its angle is the same as that of $\vec{i}$. This approximation will not affect the steady-state results.

The integral of the command voltage $\tilde{\vec{v}}(t)$ can be shown to be

$$\vec{s}(t) = \int \tilde{\vec{v}}(t)dt = \vec{w}_{RDT}(t) + \vec{\lambda}(t), \tag{23}$$

where

$$\vec{w}_{RDT}(t) = \int \vec{v}_{RDT}(t)dt. \tag{24}$$

In steady-state operation, this can be represented as follows in the rotor reference frame:

$$\vec{W}^r_{RDT} = \frac{-\mathbf{J}\vec{V}^r_{RDT}}{\Omega_{re}} = -\frac{\mathbf{J}}{\Omega_{re}}V^r_{RDT}(\|\vec{I}\|)\frac{\vec{I}}{\|\vec{I}\|} \tag{25}$$

Fig. 19 shows a block diagram of the control system used for characterization.

The characterization approach assumes that the flux linkage/current relationships of the machine possess the following (standard) symmetries:

$$\lambda^r_d(i^r_d, -i^r_q, T_r) = \lambda^r_d(i^r_d, i^r_q, T_r), \tag{26}$$

$$\lambda^r_q(i^r_d, -i^r_q, T_r) = -\lambda^r_q(i^r_d, i^r_q, T_r). \tag{27}$$

These symmetries are exploited to separate the steady-state flux linkage $\vec{\Lambda}$ from $\vec{W}_{RDT}$. This is achieved by using the current regulator to command the following two steady-state current vectors, where the direct component is the same and the sign of the quadrature component is flipped.

$$\vec{I}^r_1 = \begin{bmatrix} I^r_d \\ I^r_q \end{bmatrix}, \vec{I}^r_2 = \begin{bmatrix} I^r_d \\ -I^r_q \end{bmatrix} \tag{28}$$

and determining the corresponding integrals $\vec{S}^r_1$ and $\vec{S}^r_2$. These operating points are commanded one immediately after the other so that the rotor temperature remains relatively unchanged.

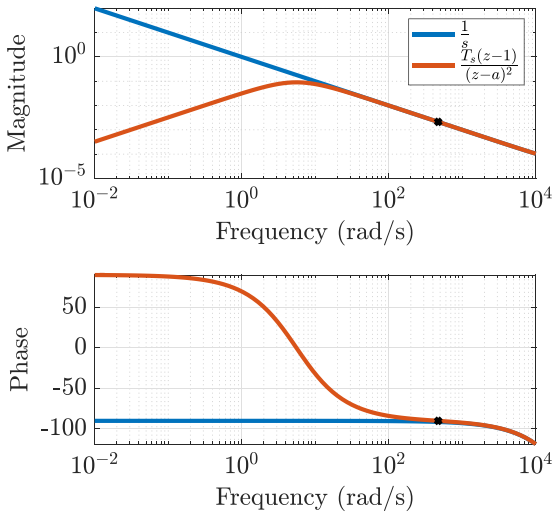

Fig. 20. Bode plots comparing numerical integrator to ideal integration, $a = 0.9994$. Crosses represent magnitude and phase at the electrical frequency used for characterization ($75Hz$).

It can then be shown that, using (23) and (25) and the symmetries in (26) and (27), the steady-state flux linkages corresponding to I^r_d and I^r_q are given by

$$\Lambda^r_d = \frac{S^r_{1d} + S^r_{2d}}{2}, \Lambda^r_q = \frac{S^r_{1q} - S^r_{2q}}{2} \tag{29}$$

1) Numerical Integration: The integration of $\vec{s}$ is done numerically using the following discrete-time transfer function:

$$\vec{S}(z) = \frac{T_s(z-1)}{(z-a)^2}\tilde{\vec{V}}(z), \tag{30}$$

where $a = 0.9994$ was chosen so that the transfer function has the same magnitude and phase shift as ideal integration at the frequency of characterization ($75Hz$), as shown in Fig. 20. The discrete-time transfer function also has zero DC gain to eliminate the effects of DC offsets on the integration.

C. Operating Points

The machine under test does not experience appreciable saturation under normal operation. Therefore, to evaluate the model over a broad range and illustrate the benefits of the proposed model, the following two data sets were collected and analyzed:

- *Test 1 Data*:
  The current i^r_q was set to zero and i^r_d was varied from -300A to 500A.
- *Test 2 Data*:
  The current i^r_q was varied from -400A to 400A and i^r_d was varied from 100A to 300A.

The resulting $\lambda^r_d - i^r_d$ relationships for Test 1 data are shown in Fig. 21 for rotor temperatures $T_1 = 60°C$ and $T_2 = 90°C$.

1) Calculation of I_{pm} and Λ_{pm}: The values of I_{pm} and Λ_{pm} were not determined in real time but calculated offline using the characterization data. The flux-linkage estimation process discussed in the prequel does not provide accurate flux-linkage

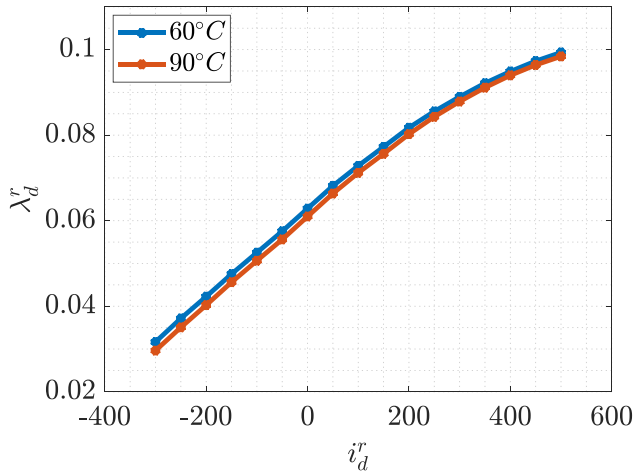

Fig. 21. Experimental λ_d^r - i_d^r characterization of UQM 145 machine for rotor temperatures $T_1 = 60°C$ and $T_2 = 90°C$, $i_q^r = 0$.

estimates when there are high levels of field weakening (i.e., large negative values of i_d^r.) This is due to the fact that, in these circumstances, the emf of the windings becomes a small fraction of the overall voltage. As a result, the estimated flux linkages become highly sensitive to errors in the estimated winding resistance, voltage drops of the inverter transistors, and deadtime, which are used to calculate the emf. Hence we cannot accurately determine the zero-flux-linkage condition as we did with the FEA study, and so another method must be used to determine the value of I_{pm}. This is achieved through the following process:

- Using the experimentally determined $\lambda_d^r - i_d^r$ data at temperature T_1, create a function which calculates $\lambda_d^r = g_{dT_1}(i_d^r + I_{pmT_1})$ for a given value of I_{pmT_1} through the use of lookup tables and linear interpolation.
- Repeat the above step for data taken at temperature T_2.
- Determine the values of I_{pm} at temperatures T_1 and T_2 simultaneously by solving the following minimization problem

$$\min_{I_{pmT1}, I_{pmT2}} \left\| g_{dT_1}\left(i_d^r + I_{pmT_1}\right) - g_{dT_2}\left(i_d^r + I_{pmT_2}\right) \right\|^2, \quad (31)$$

where $\|\cdot\|$ represents the L^2 norm.

For the baseline NL PM flux linkage model, Λ_{pm} is computed from the experimental through two different methods as described below.

Method 1: This is same method described earlier in III-B where Λ_{pm} is determined from the estimated λ_d^r when the currents are set to zero.

Method 2: This method is analogous to the one used to compute I_{pm}. Functions $f_{dT_1}(\lambda_d^r - \Lambda_{pmT_1})$ and $f_{dT_2}(\lambda_d^r - \Lambda_{pmT_2})$ are constructed for given values of Λ_{pmT_1} and Λ_{pmT_2} using the experimental data taken at temperatures T_1 and T_2, respectively. The values of the PM flux linkage at temperatures T_1 and T_2 are then determined simultaneously by solving the following minimization problem

$$\min_{\Lambda_{pmT_1}, \Lambda_{pmT_2}} \left\| f_{dT_1}\left(\lambda_d^r - \Lambda_{pmT_1}\right) - f_{dT_2}\left(\lambda_d^r - \Lambda_{pmT_2}\right) \right\|^2. \quad (32)$$

The solver fmincon in MATLAB was used to solve the optimization problems to compute I_{pm} and Λ_{pm}. The values of I_{pm} and Λ_{pm} for both rotor temperartures ($T_1 = 60°C$ and $T_2 = 90°C$) from the experimental results are shown in Table VIII.

TABLE VIII
EXPERIMENTAL I_{pm} AND Λ_{pm} VALUES

T_r (°C)	I_{pm} (A)	$\Lambda_{pm}(V-s)$	
		Method 1	Method 2
60	603.6	0.0628	0.0625
90	585.4	0.0610	0.0609

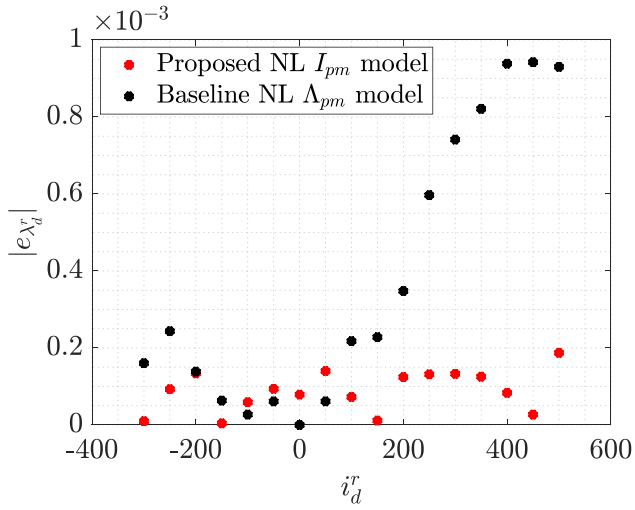

Fig. 22. Absolute errors in λ_d^r for proposed NL PM current and baseline NL PM flux linkage models at $T_r = 90°$C using Method 1 for Λ_{pm} calculation, Test 1 data experimental results.

2) Comparison Results: The models were compared using the same technique used in III-B for the FEA results. Fig. 22 shows the absolute error in λ_d^r for the PM current model and NL PM flux linkage model for Test 1 data, where the value of Λ_{pm} for the nonlinear PM flux linkage model at temperature T_2 was computed using Method 1. While the models show similar accuracy in the linear region (i.e., negative i_d^r excitation), one can distinctly observe the improved accuracy of the proposed model in the region of magnetic saturation.

Fig. 23 compares the absolute error in λ_d^r when Λ_{pm} for the NL PM flux linkage model is computed using Method 2 for the Test 1 data. In this case, the proposed model shows better accuracy in both the nonlinear and linear regions.

Figs. 24 and 25 show the results for Test 2 data. Subplots (a), (b) in Figs. 24 and 25 highlight the absolute error in λ_d^r for the NL PM current model and NL PM flux linkage model using Methods 1 and 2 for Λ_{pm} calculation respectively. The proposed model demonstrates higher accuracy in both cases. We observe a similar model error in case of λ_q^r (subplots (c), (d) in Figs. 24

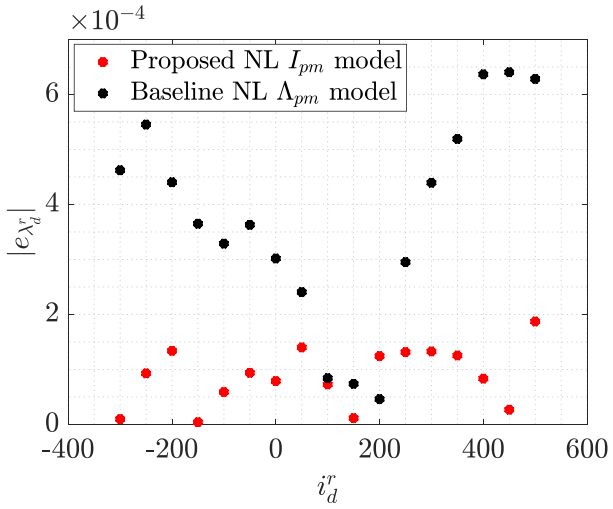

Fig. 23. Absolute errors in λ_d^r for proposed NL PM current and baseline NL PM flux linkage models at $T_r = 90°$C using Method 2 for Λ_{pm} calculation, Test 1 data experimental results.

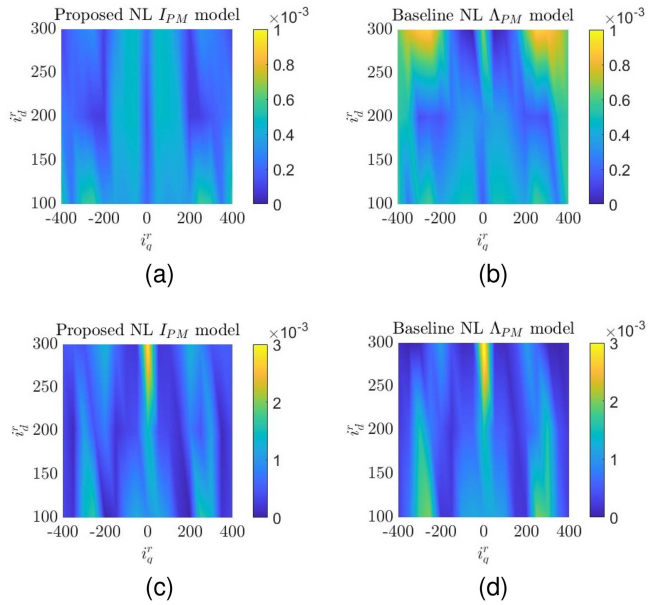

Fig. 24. Absolute errors in λ_d^r (top) and λ_q^r (bottom) at $T_r = 90°C$ using Method 1 for Λ_{pm} calculation, Test 2 data experimental results for the proposed (a, c) and baseline (b, d) models.

and 25), which is consistent with the observation from the FEA results.

V. Conclusion

A machine model for PMSMs that captures the effects of magnetic saturation and rotor temperature variations has been proposed, and its efficacy and ease of implementation are demonstrated. The main contribution of the proposed model is the decoupling of the effects of magnetic saturation and rotor temperature variation, the latter being captured in a PM current parameter I_{pm}. This parameter can be adaptively estimated,

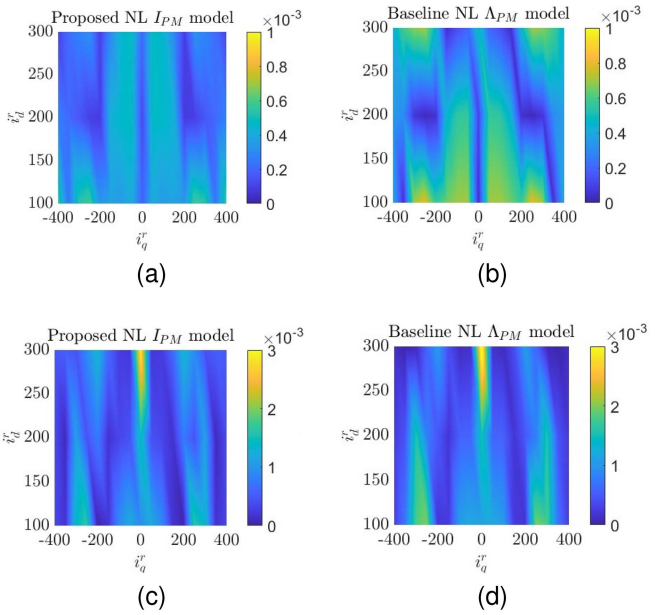

Fig. 25. Absolute errors in λ_d^r (top) and λ_q^r (bottom) at $T_r = 90°C$ using Method 2 for Λ_{pm} calculation, Test 2 data experimental results for the proposed (a, c) and baseline (b, d) models.

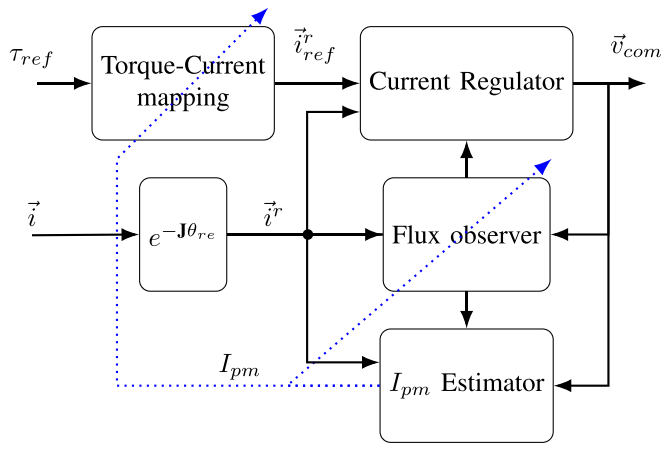

Fig. 26. Example torque regulator based on proposed magnetics model.

thereby avoiding the need for rotor temperature measurement. The proposed model is validated using FEA simulation for an interior permanent magnet machine design, a distributed winding SMPM design, and a concentrated winding SMPM design, and shows high accuracy at different rotor temperatures when compared with a nonlinear PM flux linkage model. Experimental results also confirm that the proposed model is more accurate than the nonlinear PM flux linkage model.

Future work will involve the development of a torque regulator based upon the proposed model, such as the one shown in Fig. 26. In such a scheme, the proposed model will be used to calculate reference currents that accurately produce the command torque, and could also assist in flux linkage estimation to accurately compensate the speed-dependent cross-coupling terms in a field-oriented control strategy. An adaptive estimator will be designed

to determine the PM current in real time, thereby capturing the effects of rotor temperature variations.

REFERENCES

[1] C. C. Chan, "The state of the art of electric, hybrid, and fuel cell vehicles," *Proc. IEEE*, vol. 95, no. 4, pp. 704–718, Apr. 2007.

[2] Z. Yang, F. Shang, I. P. Brown, and M. Krishnamurthy, "Comparative study of interior permanent magnet, induction, and switched reluctance motor drives for EV and HEV applications," *IEEE Trans. Transport. Electrific.*, vol. 1, no. 3, pp. 245–254, Oct. 2015.

[3] G. Pellegrino, A. Vagati, P. Guglielmi, and B. Boazzo, "Performance comparison between surface-mounted and interior pm motor drives for electric vehicle application," *IEEE Trans. Ind. Electron.*, vol. 59, no. 2, pp. 803–811, Feb. 2012.

[4] B. Bilgin et al., "Making the case for electrified transportation," *IEEE Trans. Transport. Electrific.*, vol. 1, no. 1, pp. 4–17, Jun. 2015.

[5] J. Weimer, "The role of electric machines and drives in the more electric aircraft," in *Proc. IEEE Int. Electric Mach. Drives Conf.*, 2003, vol. 1, pp. 11–15.

[6] R. Krishnan and A. Bharadwaj, "A comparative study of various motor drive systems for aircraft applications," in *Proc. Conf. Rec. IEEE Ind. Appl. Soc. Annu. Meeting*, 1991, pp. 252–258.

[7] B. Sarlioglu and C. T. Morris, "More electric aircraft: Review, challenges, and opportunities for commercial transport aircraft," *IEEE Trans. Transport. Electrific.*, vol. 1, no. 1, pp. 54–64, Jun. 2015.

[8] T. M. Jahns, G. B. Kliman, and T. W. Neumann, "Interior permanent-magnet synchronous motors for adjustable-speed drives," *IEEE Trans. Ind. Appl.*, vol. IA-22, no. 4, pp. 738–747, Jul. 1986.

[9] P. B. Reddy, A. El-Refaie, K.-K. Huh, J. K. Tangudu, and T. M. Jahns, "Comparison of interior and surface pm machines equipped with fractional-slot concentrated windings for hybrid traction applications," in *Proc. IEEE Energy Convers. Congr. Expo.*, 2011, pp. 2252–2259.

[10] A. Tüysüz, F. Meyer, M. Steichen, C. Zwyssig, and J. W. Kolar, "Advanced cooling methods for high-speed electrical machines," *IEEE Trans. Ind. Appl.*, vol. 53, no. 3, pp. 2077–2087, May/Jun. 2017.

[11] D. Lee et al., "Detailed design and prototyping of a high power density slotless PMSM," *IEEE Trans. Ind. Appl.*, vol. 59, no. 2, pp. 1719–1727, Mar./Apr. 2023.

[12] A. M. El-Refaie et al., "Advanced high power-density interior permanent magnet motor for traction applications," in *Proc. IEEE Energy Convers. Congr. Expo.*, 2013, pp. 581–590.

[13] "Sintered neodymium-iron-boron magnets," Arnold Magnetic Technologies, rev. 210607. (n.d.). [Online]. Available: https://www.arnoldmagnetics.com/wp-content/uploads/2017/11/N35UH-151021.pdf

[14] S. Li, B. Sarlioglu, S. Jurkovic, N. R. Patel, and P. Savagian, "Analysis of temperature effects on performance of interior permanent magnet machines for high variable temperature applications," *IEEE Trans. Ind. Appl.*, vol. 53, no. 5, pp. 4923–4933, Sep./Oct. 2017.

[15] S. Li, B. Sarlioglu, S. Jurkovic, N. R. Patel, and P. Savagian, "Comparative analysis of torque compensation control algorithms of interior permanent magnet machines for automotive applications considering the effects of temperature variation," *IEEE Trans. Transport. Electrific.*, vol. 3, no. 3, pp. 668–681, Sep. 2017.

[16] S. Li, D. Han, and B. Sarlioglu, "Modeling of interior permanent magnet machine considering saturation, cross coupling, spatial harmonics, and temperature effects," *IEEE Trans. Transport. Electrific.*, vol. 3, no. 3, pp. 682–693, Sep. 2017.

[17] I. Voncilă, I. Paraschiv, and M. Costin, "The influence of saturation on the performance of PMSM," in *Proc. 7th Int. Symp. Elect. Electron. Eng.*, 2021, pp. 1–6.

[18] T. Sebastian, "Temperature effects on torque production and efficiency of pm motors using NDFEB magnets," *IEEE Trans. Ind. Appl.*, vol. 31, no. 2, pp. 353–357, Mar./Apr. 1995.

[19] Y.-S. Kim and S.-K. Sul, "Torque control strategy of an IPMSM considering the flux variation of the permanent magnet," in *Proc. IEEE Ind. Appl. Annu. Meeting*, 2007, pp. 1301–1307.

[20] P. Pillay and R. Krishnan, "Modeling of permanent magnet motor drives," *IEEE Trans. Ind. Electron.*, vol. 35, no. 4, pp. 537–541, Nov. 1988.

[21] P. Pillay and R. Krishnan, "Modeling, simulation, and analysis of permanent-magnet motor drives. I. The permanent-magnet synchronous motor drive," *IEEE Trans. Ind. Appl.*, vol. 25, no. 2, pp. 265–273, Mar./Apr. 1989.

[22] T. Sebastian, G. Slemon, and M. Rahman, "Modelling of permanent magnet synchronous motors," *IEEE Trans. Magn.*, vol. 22, no. 5, pp. 1069–1071, Sep. 1986.

[23] F. Parasiliti and P. Poffet, "A model for saturation effects in high-field permanent magnet synchronous motors," *IEEE Trans. Energy Convers.*, vol. 4, no. 3, pp. 487–494, Sep. 1989.

[24] S. L. Kellner and B. Piepenbreier, "General PMSM d,q-model using optimized interpolated absolute and differential inductance surfaces," in *Proc. 2011 IEEE Int. Electric Mach. Drives Conf.*, 2011, pp. 212–217.

[25] X. Sun and X. Xiao, "Precise non-linear flux linkage model for permanent magnet synchronous motors based on current injection and bivariate function approximation," *IET Electric Power Appl.*, vol. 14, no. 11, pp. 2044–2050, 2020.

[26] K. Drobnič, L. Gašparin, and R. Fišer, "Fast and accurate model of interior permanent-magnet machine for dynamic characterization," *Energies*, vol. 12, no. 5, 2019, Art. no. 783. [Online]. Available: https://www.mdpi.com/1996-1073/12/5/783

[27] K. Rahman and S. Hiti, "Identification of machine parameters of a synchronous motor," *IEEE Trans. Ind. Appl.*, vol. 41, no. 2, pp. 557–565, Mar./Apr. 2005.

[28] B. Stumberger, G. Stumberger, D. Dolinar, A. Hamler, and M. Trlep, "Evaluation of saturation and cross-magnetization effects in interior permanent-magnet synchronous motor," *IEEE Trans. Ind. Appl.*, vol. 39, no. 5, pp. 1264–1271, Sep./Oct. 2003.

[29] N. Bianchi and S. Bolognani, "Magnetic models of saturated interior permanent magnet motors based on finite element analysis," in *Proc. Conf. Rec. IEEE Ind. Appl. Conf., 33rd IAS Annu. Meeting*, 1998, vol. 1, pp. 27–34.

[30] D. Hu, Y. M. Alsmadi, and L. Xu, "High-fidelity nonlinear IPM modeling based on measured stator winding flux linkage," *IEEE Trans. Ind. Appl.*, vol. 51, no. 4, pp. 3012–3019, Jul./Aug. 2015.

[31] J. G. Cintron-Rivera, A. S. Babel, E. E. Montalvo-Ortiz, S. N. Foster, and E. G. Strangas, "A simplified characterization method including saturation effects for permanent magnet machines," in *Proc. 20th Int. Conf. Elect. Mach.*, 2012, pp. 837–843.

[32] T. Herold, D. Franck, E. Lange, and K. Hameyer, "Extension of a d-q model of a permanent magnet excited synchronous machine by including saturation, cross-coupling and slotting effects," in *Proc. IEEE Int. Electric Mach. Drives Conf.*, 2011, pp. 1363–1367.

[33] K. J. Meessen, P. Thelin, J. Soulard, and E. A. Lomonova, "Inductance calculations of permanent-magnet synchronous machines including flux change and self- and cross-saturations," *IEEE Trans. Magn.*, vol. 44, no. 10, pp. 2324–2331, Oct. 2008.

[34] X. Chen, J. Wang, B. Sen, P. Lazari, and T. Sun, "A high-fidelity and computationally efficient model for interior permanent-magnet machines considering the magnetic saturation, spatial harmonics, and iron loss effect," *IEEE Trans. Ind. Electron.*, vol. 62, no. 7, pp. 4044–4055, Jul. 2015.

[35] C. Choi, W. Lee, S.-O. Kwon, and J.-P. Hong, "Experimental estimation of inductance for interior permanent magnet synchronous machine considering temperature distribution," *IEEE Trans. Magn.*, vol. 49, no. 6, pp. 2990–2996, Jun. 2013.

[36] G. Luo, R. Zhang, Z. Chen, W. Tu, S. Zhang, and R. Kennel, "A novel nonlinear modeling method for permanent-magnet synchronous motors," *IEEE Trans. Ind. Electron.*, vol. 63, no. 10, pp. 6490–6498, Oct. 2016.

[37] X. Chen, J. Wang, and A. Griffo, "A high-fidelity and computationally efficient electrothermally coupled model for interior permanent-magnet machines in electric vehicle traction applications," *IEEE Trans. Transport. Electrific.*, vol. 1, no. 4, pp. 336–347, Dec. 2015.

[38] P. Ioannou and J. Sun, *Robust Adaptive Control*. Upper Saddle River, NJ, USA: Prentice Hall, Inc., 2003.

[39] S. Lin, X. Li, T. Wu, L. Chow, Z. Tang, and S. Stanton, "Temperature dependent reduced order IPM motor model based on finite element analysis," in *Proc. IEEE Int. Electric Mach. Drives Conf.*, 2015, pp. 543–549.

[40] F. Poltschak and W. Amrhein, "A dynamic nonlinear model for permanent magnet synchronous machines," in *Proc. IEEE Int. Symp. Ind. Electron.*, 2008, pp. 724–729.

[41] H. Cai and D. Hu, "On PMSM model fidelity and its implementation in simulation," in *Proc. IEEE Energy Convers. Congr. Expo.*, 2018, pp. 1674–1681.

[42] T. Sebastian and G. Slemon, "Transient modeling and performance of variable-speed permanent-magnet motors," *IEEE Trans. Ind. Appl.*, vol. 25, no. 1, pp. 101–106, Jan./Feb. 1989.

[43] A. B. Dehkordi, A. Gole, and T. Maguire, "Permanent magnet synchronous machine model for real-time simulation," 2005. [Online]. Available: https://api.semanticscholar.org/CorpusID:15953835

[44] M. Gierczynski and L. M. Grzesiak, "Comparative analysis of the steady-state model including non-linear flux linkage surfaces and the simplified linearized model when applied to a highly-saturated permanent magnet synchronous machine—evaluation based on the example of the BMW I3 traction motor," *Energies*, vol. 14, no. 9, 2021, Art. no. 2343. [Online]. Available: https://www.mdpi.com/1996-1073/14/9/2343
[45] P. Alvarez, M. Satrústegui, I. Elósegui, and M. Martinez-Iturralde, "Review of high power and high voltage electric motors for single-aisle regional aircraft," *IEEE Access*, vol. 10, pp. 112989–113004, 2022.
[46] E. Armando, R. I. Bojoi, P. Guglielmi, G. Pellegrino, and M. Pastorelli, "Experimental identification of the magnetic model of synchronous machines," *IEEE Trans. Ind. Appl.*, vol. 49, no. 5, pp. 2116–2125, Sep./Oct. 2013. [Online]. Available: https://api.semanticscholar.org/CorpusID:13836038
[47] G. Pellegrino, B. Boazzo, and T. M. Jahns, "Magnetic model self-identification for PM synchronous machine drives," *IEEE Trans. Ind. Appl.*, vol. 51, no. 3, pp. 2246–2254, May/Jun. 2015.

Kishan Srinivasan (Graduate Student Member, IEEE) received the B.Tech. degree in electrical engineering from Pandit Deendayal Energy University, Gandhinagar, Gujarat, India, in 2019, and the M.S. degree in 2021 from the University of Michigan, Ann Arbor, MI, USA, where he is currently working toward the Ph.D. degree with the Department of Electrical Engineering and Computer Science. His research interests include power electronics and electric machines and drives.

Fanny A. Pinto Delgado (Member, IEEE) received the B.Sc. degree in electrical engineering from Universidad Simon Bolivar, Caracas, Venezuela, in 2014, the M.Sc. and Ph.D. degrees in electrical engineering systems from the University of Michigan, Ann Arbor, MI, USA, in 2017 and 2021, respectively. She has worked under the guidance of Professor Heath Hofmann and Professor Jing Sun. She is currently with Mercedes-Benz Research and Development North America. Her research interests include condition monitoring and control of electric machines. She has been a IEEE Student Member since 2018.

Heath F. Hofmann (Fellow, IEEE) received the Ph.D. degree in electrical engineering and computer science from the University of California at Berkeley, Berkeley, CA, USA, in 1998. He is currently a Professor with the University of Michigan, Ann Arbor, MI, USA. He has authored approximately five dozen papers in refereed journals, and currently holds eight patents. His research interests include power electronics, specializing in the design, simulation, and control of electromechanical systems.

Jing Sun (Fellow, IEEE) received the Ph.D. degree from the University of Southern California at Los Angeles, Los Angeles, CA, USA, in 1989. She is currently the Michael G. Parsons Collegiate Professor with the Department of Naval Architecture and Marine Engineering, joint appointments with the Department of Electrical Engineering and Computer Science, and the Department of Mechanical Engineering, University of Michigan, Ann Arbor, MI, USA. Her research interests include modeling, control, and optimization of dynamic systems, with applications to marine and automotive systems. She was the recipient of the 2003 IEEE Control System Technology Award. Dr. Sun is also a fellow of the National Academy of Inventors, International Federation of Automatic Control (IFAC), and the Society of Naval Architects and Marine Engineers.